14th International Symposium on Turbulence and Shear Flow Phenomena (TSFP14)
Heidelberg, Germany, July 28–31, 2026

MORPHING SURFACE ACTUATION OF A TURBULENT BOUNDARY LAYER WITH VLSM-MATCHED TRAVELING WAVES

Alexey Zhelebovskiy
Faculty of Aerospace Engineering
Technion Israel Institute of Technology
Haifa, 32000 Israel

Mitul Luhar
Dept. of Aerospace and Mechanical Engineering
University of Southern California
Los Angeles, CA 90089

Ian Jacobi
Faculty of Aerospace Engineering
Technion Israel Institute of Technology
Haifa, 32000 Israel
ijacobi@technion.ac.il

ABSTRACT

A mechanical morphing surface was developed for operation in a high-speed water tunnel facility to target large-scale motions (LSMs) in a turbulent boundary layer via wall perturbations. The morphing surface consists of hundreds of individually actuated servo motors moving in concert to produce arbitrary 3D wall disturbances with outer scale resolution. We describe the design and operation of the morphing surface and then utilize it to generate a traveling-wave, large-scale wall perturbation with phase speed matched to the local mean velocity in the near-wall region of the boundary layer. The large-scale flow field was measured with time-resolved, planar particle-image velocimetry (PIV), and the space-time spectrum of the streamwise turbulence was compared across wall-normal locations to identify the dispersive behavior of the traveling wave input. The traveling wave perturbation was also contrasted with a static wavy wall with matched wavelength. The initial measurements presented here demonstrate the utility of a mechanical morphing surface for assessing the sensitivity of wall-bounded turbulence to traveling perturbations of varying phase-speeds.

BACKGROUND

Turbulent flow over complex, morphing geometries is fundamental to understanding a wide range of environmental flows, from sand dunes and ocean waves to river bed dynamics (Belcher & Hunt, 1998) and has received more recent attention in engineering applications for drag reduction and flow control. Wavy walls were first studied in static configurations, where local flow separation results in a recirculation zone and a shear layer downstream of each wavy ‘hill’ in the region of flow near the wall. Wavy walls have also been observed to generate significant spanwise-oriented, secondary vortices and a redirection of turbulent kinetic energy into the spanwise direction (De Angelis *et al.*, 1997). The resulting flow reorganization influences the meandering of large-scale coherent structures (Kruse *et al.*, 2003). Dynamic wavy walls have mostly been studied in the context of bedform dynamics, either in field observations or simulations of mobile bedforms using gravel (Lee *et al.*, 2022). However, artificial, dynamic wall deformation in the form of a traveling wave has been tested in airfoils to suppress stall (Akbarzadeh & Borazjani, 2020) and in channels to reduce drag (Nabae *et al.*, 2020). With a few notable exceptions, these studies have not exploited more recent insights that emphasize the importance of large-scale motions (LSMs) and very-large scale motions (VLSMs) in organizing wall-bounded flows.

LSMs have been widely understood to exert an important organizing influence on smaller scale coherent motions. These influences have been quantified in terms of an amplitude modulation coefficient (Mathis *et al.*, 2009) and have been employed in models to predict near-wall, small-scale fluctuations based on outer-layer, large-scale structures (Mathis *et al.*, 2011). Marusic *et al.* (2021) targeted these VLSM scales in a spanwise traveling-wave wall actuation to produce energy-efficient drag reduction by exploiting the organizing effects of the large-scales. Because their reported drag reduction has recently been challenged in computational work by Gatti *et al.* (2025), the general approach of targeting large-scale motions is in need of further exploration.

By examining the amplitude modulation coefficent, R, used to quantify the relationships between large- and small-scales, Cui & Jacobi (2023) and Cui & Jacobi (2025) suggested that what is really being measured by R is convective velocity differences between interacting large- and small-scale motions, and not merely the presence of non-linear interactions. The convective velocities of large-scale coherent structures are also essential ingredients in the resolvent-based modeling of turbulence, in which a super-position of critical modes, each convecting at the local mean velocity of the flow, can be used to represent canonical wall-bounded flows as well as compliant walls (Luhar *et al.*, 2015) and drag-reducing riblet surfaces (Chavarin & Luhar, 2020).

In this study, we designed and built a mechanical, morphing wall surface that can generate dynamic 3D surface disturbances of arbitrary form, and we utilized the surface to perturb a turbulent boundary layer with a traveling wave form at the scale of a LSM, with phase speed matched to the near-wall local mean velocity. The design and testing of the morphing wall are presented in the next section, followed by results from water-tunnel, boundary layer experiments for the

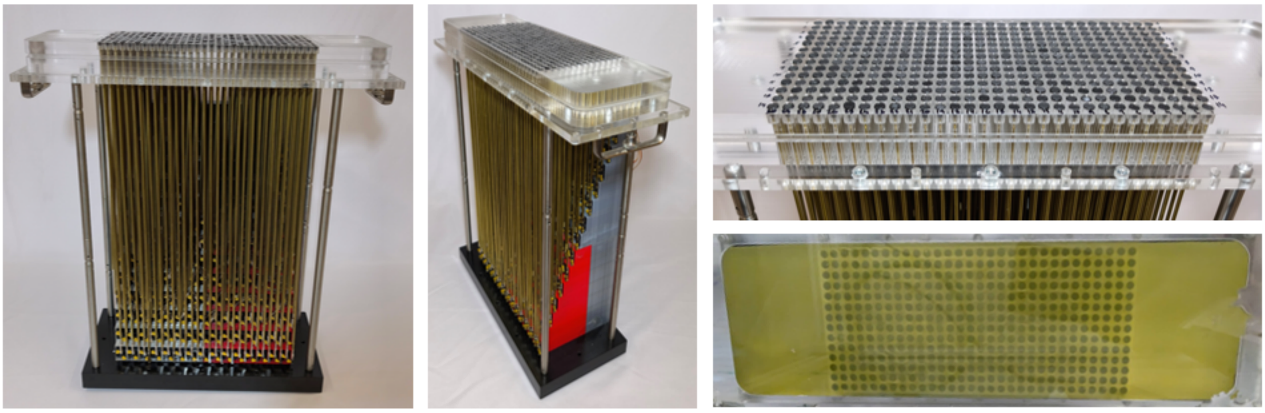

Figure 1. The morphing surface plate and actuator array. The servo actuators were staggered in steps to improve the spatial resolution at the top of the plate, and each servo was connected to a piston that moves vertically in the flat plate via a slider-crank linkage. The plate with the pistons is shown in the top right, and was sealed with a latex membrane to create an approximately continuous surface over the discrete actuators, shown in the bottom right after installation in the ceiling of the high speed water tunnel.

traveling-wave wall perturbation and a static wavy wall with matched wavelength. The final section discusses the effect of the traveling wave perturbation on the space-time energy spectrum, and implications for studying the sensitivity of the turbulent boundary layer to LSM perturbations with varying phase-speeds.

MORPHING SURFACE DESIGN

The morphing surface was constructed from an array of discrete, mechanical actuators located on a 500×150mm plate installed on the ceiling of the test section of a water tunnel and was designed to generate highly localized, three-dimensional surface actuation. The actuators were mounted in an acrylic grid, 26 actuators across in the streamwise direction and 14 across in the spanwise direction with a spacing of $\ell = 10$mm in both directions in a Cartesian grid pattern. The top of each actuator was a round piston with a diameter of 7.6 mm. The actuators were separated from the water flow with a flexible latex membrane of thickness 0.25mm bonded to the edges of acrylic plate and actuator pistons to form a continuous surface over the discrete actuator elements. The actuator surface, with and without the membrane, is shown in figure 1, along with the frame containing the motors.

The actuator pistons were driven by micro-servo motors (Pololu DSM44), which have a maximum speed of 140RPM. The driving motors and the pistons were connected with a slider-crank linkage. The crank length, l_1, was fixed for all actuators to 5 mm, while the slider length, l_2, varied in the wall-normal direction from 100 to 500 mm in order to accommodate the staggered placement of the driving motors. For these ratios ($l_1/l_2 = 0.01$–0.05), the resulting motion deviated only weakly from a purely sinusoidal profile, with second-harmonic distortions below approximately 2.5% of the stroke amplitude. Motor actuation allows varying the crank angle by $\pm 15^\circ$ from horizontal, which translates into vertical piston motion of ± 1.3mm. The pistons were tapered conically (at 20°) and attached to the slider via a ball joint of diameter 5 mm which allows the piston to tilt under the tension of the membrane, thereby obtaining a closer approximation to a continuous surface variation. Figure 2 illustrates the generation of a sinusoidal wave via the vertical motion of the pistons under the membrane.

The real-time position of the servo motors was obtained from each motor's internal potentiometer and used as an input in a proportional-integral (PI) control scheme to regulate the motor position. At each time instant, the desired surface configuration was sent from a computer via a CAN bus to 26 controller boards, each controlling a spanwise row of 14 actuators. The initial experiments, described below, achieved a vertical piston velocity of approximately 25 mm/s (as measured by high speed camera), although this value was chosen conservatively and likely underestimates the maximum achievable velocity based on motor specifications.

Individual piston centers were spaced at $\ell = 10$mm increments, which yields a minimum wavelength of 20mm for two actuation points per wavelength (or 50mm for more continuous, five-point control). In the water tunnel facility, the boundary layer thickness tends to range from 10-25 mm, depending on streamwise position and free-stream velocity, and thus the morphing wall was able to produce traveling wave perturbations that can target natural VLSMs in the flow. The initial tests, reported here, were performed at relatively low Reynolds number to demonstrate effect of injecting LSM-sized traveling waves into a turbulent boundary layer without a significant amount of turbulent kinetic energy at large scales.

BOUNDARY LAYER EXPERIMENTS

The complete morphing surface assembly was installed along the ceiling of our high speed water tunnel facility, which has a 20 cm $\times$ 20 cm $\times$ 200 cm test section and can achieve free stream velocities in the range of 0.1 to 8.0 m/s, with a turbulence intensity of less than 1%. For the initial experiments, the morphing surface was installed closer to the entrance of the test-section to reduce the scale of LSMs and allow for a large field of view relative to the injected LSMs. The leading edge of the membrane was located 250 mm downstream of the leading edge of the test section, and the center of the first spanwise row of actuators was located 105 mm downstream of the membrane leading edge. Planar PIV measurements were performed in streamwise/wall-normal plane at the spanwise center of plate, starting $75mm$ downstream of the membrane, with a field of view of 106×33 mm. The orientation of the measurement domain is sketched in the dashed lines in figure 2.

The flow was illuminated with a 527 nm wavelength laser

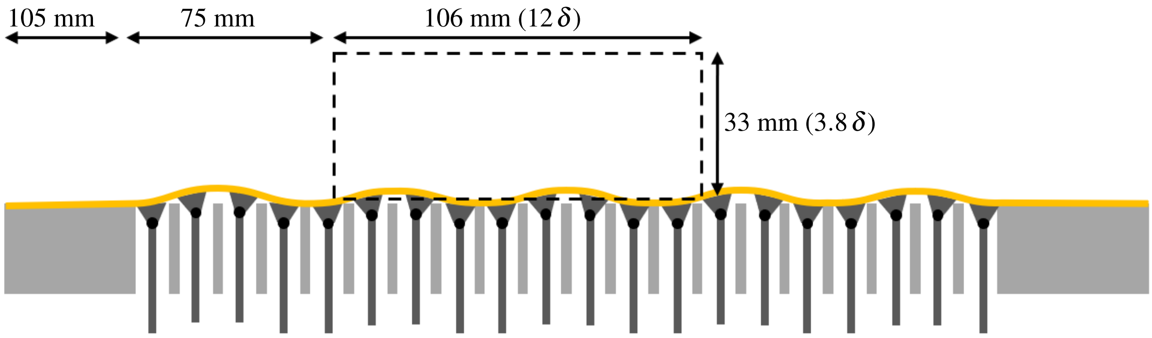

Figure 2. A sketch of the morphing surface with the PIV field of view marked (dashed line), along with the downstream distances from the first row of pistons and from the leading edge of the membrane. The illustration is not drawn to scale, since the individual piston spacing is 10 mm. The boundary layer thickness for the flat wall case is $\delta = 8.8$ mm.

sheet produced by a dual-pulse laser (Litron LD30-527) and imaged by high-speed camera (Phantom VEO-440L, 2560 × 1600 pixels) with sample rate 240 Hz. The duration of each recording was 12.3s and ten recordings were obtained for each of three surface conditions: flat wall, static wavy wall, and traveling wave.

All measurements were performed with a freestream velocity, $U_\infty = 1.08$ m/s. For the flat wall case, all actuators were calibrated to be level with the piston frame. The resulting boundary layer had a boundary layer thickness, $\delta \approx 8.8$mm, based on the δ_{99} definition, and a friction velocity inferred via the Clauser method of $u_\tau \approx 0.05$ m/s, resulting in a friction Reynolds number at this upstream position of $\mathrm{Re}_\tau \approx 437$, which is too low to observe natural VLSMs, but still exhibits some large-scale energetic content, as shown in the premultiplied spectral energy map in figure 3. Most of the energy is associated with the near wall cycle, with a significant weakening towards the LSMs and VLSMs, and thus these experiments focused primarily on the injection of artificial large-scales via the morphing surface and the difference between static and traveling wave perturbation schemes.

The flow was perturbed with a spanwise-uniform, streamwise-varying sinusoidal waveform (using 10 of the 14 columns of actuators in the spanwise direction). For the traveling-wave perturbation, the wave-form was defined as $\eta(x,t) = a[1+\sin(kx-\omega t)]$ with wavenumber 0.126 mm^{-1} (wavelength, $\lambda = 50$ mm), amplitude $a = 0.7$ mm, and frequency $\omega = 50.3$ rad/s ($f = 8$ Hz), resulting in a phase speed of $c = \omega/k \approx 0.4$ m/s. The waveform never descends below the flat wall height, which is defined as $y = 0$. Therefore, for the perturbed flow cases, the velocity field obtained from the PIV is masked to exclude the region $y < 2a$, in which the waviness exists. The rms amplitude of the waveform is then $a_{rms} = \sqrt{3/2}a \approx 0.86$mm, or $\delta/a_{rms} \approx 10.2$, which is too high to be considered roughness by the standard criteria (Jiménez, 2004) and is therefore just a wavy wall. We also measured the flow over a static wavy wall with the same wavenumber, in which the frequency was set to zero. Table 1 reports the basic flow statistics and perturbation parameters for all three cases.

The instantaneous velocity field measured by PIV was decomposed into a time-averaged flow, a time-varying base flow that is phase-locked to the wall deformation, and turbulent fluctuations about the base flow, following the standard 'triple decomposition' of Reynolds & Hussain (1972). Figure 4 shows the statistical profiles of the streamwise velocity component, excluding the region within the waviness itself, for the three flow scenarios. The mean velocity profiles, $\overline{u}$, are shown

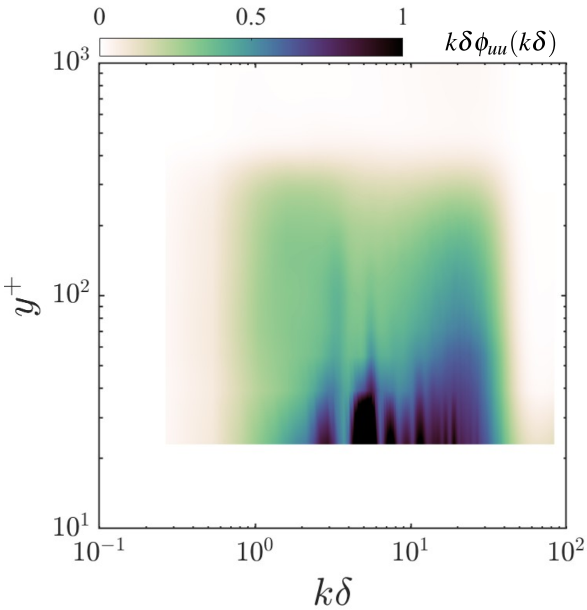

Figure 3. The pre-multiplied streamwise spectral density for the flat-wall configuration at $\mathrm{Re}_\tau \approx 437$, showing relatively little large-scale energy content.

in panel (a), the turbulence intensity, u' in (b), and the diagnostic plot (Alfredsson *et al.*, 2009) in (c).

The greatest mean velocity suppression appears in the static waviness, where the roughness layer is significantly thicker. The static waviness also exhibits a higher turbulence intensity, with a significant amount of near-wall turbulence displaced into the outer region. The traveling wave case falls between the static and flat wall profiles. The diagnostic plot allows for a comparison of the profiles without dependence on the wall-location, and it, too, shows that the static waviness dominates the other flow scenarios with respect to the turbulence intensity (relative to the local mean velocity at each height).

The phase-locked, streamwise velocity fields were calculated by binning the 30 image pairs, recorded during each period of the traveling wave oscillation, over the 98 periods per recording and then over the ten recordings in each experiment. Each bin was then assigned a phase denoted ϕ. The streamwise velocity field for one phase is shown in figure 5(a), aligned vertically with an image of the morphing surface at the

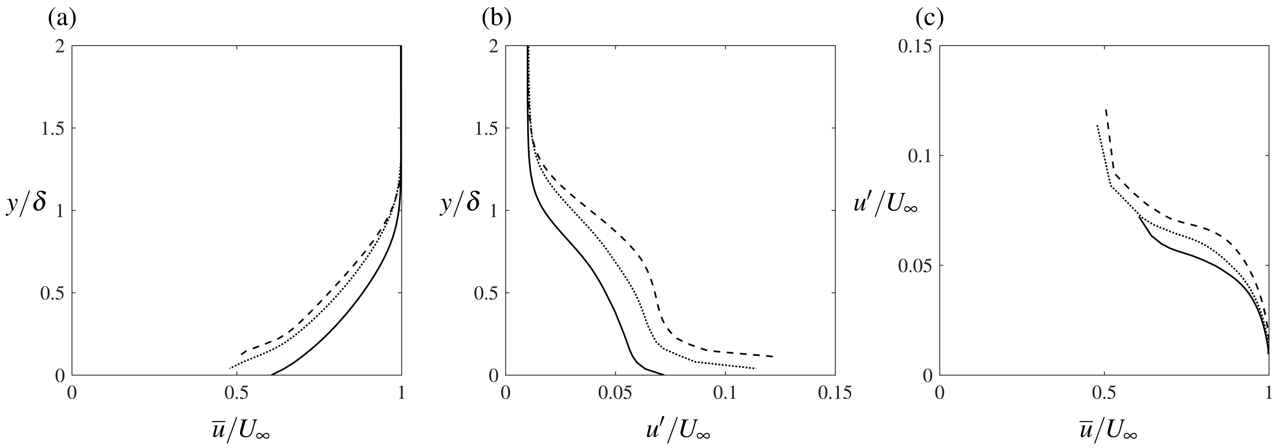

Figure 4. Statistical profiles of the streamwise velocity component for all three flow scenarios: flat wall (solid line), static wavy wall (dashed line), and traveling wave (dotted line). (a) Mean velocity profiles $\overline{u}$, (b) turbulence intensity u', and (c) diagnostic plot.

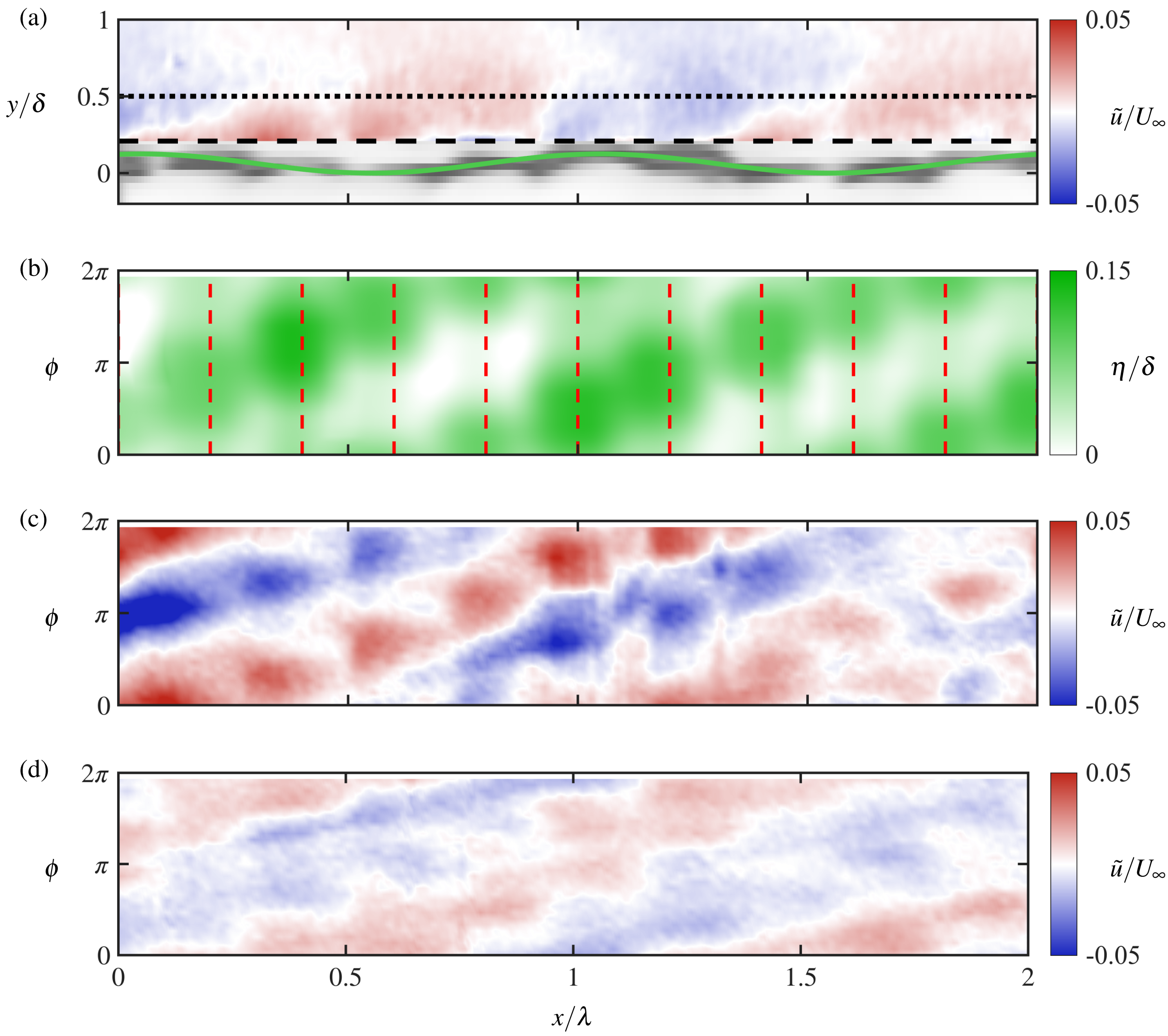

Figure 5. (a) Phase-locked, streamwise velocity field, $\tilde{u}$ for phase $\phi = \pi/2$, with the surface height, η, shown below in green, and two slices marked by the dashed and dotted black lines; (b) the morphing surface height, η along the streamwise direction for all phases; (c) a slice of the phase-locked streamwise velocity, $\tilde{u}$, at $y/\delta \approx 0.2$, for all phases; and (d) the other slice at $y/\delta \approx 0.5$ for all phases.

	Flat	Static	Traveling
δ [mm]	8.8	9.0	8.3
k [mm^{-1}]	–	0.13	0.13
$k\delta$	–	1.14	1.05
ω [rad/s]	–	–	50.3
$\omega\delta/U_\infty$	–	–	0.39

Table 1. Boundary layer and perturbation parameters for the three flow scenarios. All cases have a free-stream velocity of $U_\infty \approx 1.08$ m/s. The flat wall case has $\mathrm{Re}_\tau \approx 437$. The boundary layer thickness δ is δ_{99}.

corresponding phase (and a green line indicating the idealized, continuous surface shape profile, η, which was the command input to the morphing surface controller).

High- and low-speed, downstream inclined coherent structures appear organized over the traveling wave surface, with low-speed structures over the peaks and high-speed structures over the troughs. The structures appear to extend across nearly the entire boundary layer thickness, indicating a prominent vertical component to the wall excitation. The downstream inclination and phase-locking with the wall are both consistent with an attached eddy picture of these large-scale motions.

In figure 5(b), we constructed a space-phase map of the surface elevation, where the peaks appear in levels of green, tilted according to the phase speed. The red dashed lines mark the locations of individual actuators, and therefore it is clear that the actuator pistons still retain some of their discrete shape, despite the elastic membrane designed to smooth over the large-scale wave forms. Tracing along a single red line indicates the time trace of a single actuator over its average period.

We constructed similar space-phase maps for the phase-averaged, streamwise velocity component in figures 5(c) and (d), corresponding to wall-parallel slices at the two wall-normal locations marked by dashed and dotted black lines in figure 5(a). Here, too, we observe that the individual actuators imprint their discrete shape onto the large-scale momentum wave forms, and that this discretization appears to persist even far from the wall itself. Also, the inclination of the velocity modes in the space-phase maps is not perfectly uniform across a spatial wavelength (i.e. the slopes of the peaks and troughs are not uniform), thus indicating some dispersion in the phase speeds between peaks and troughs of each mode.

SPACE-TIME SPECTRAL EFFECTS

Space-time spectral analysis of the large-scales was used to study modifications to the distribution of phase velocities due to the morphing wall. Figure 6 shows the two-dimensional space time spectral maps for the three flow scenarios (columns) at different wall-normal positions (rows). The wall normal positions were selected such that the local mean velocity was equal across all three flow scenarios, neglecting the substantial difference in y-location that this entails, due to the complexity of measuring the velocity field within the waviness. The actuation wavelength is marked as a vertical line for the static wavy wall case, and the actuation phase speed is marked as a circle for the traveling wall case.

The wall perturbation exerts a significant spectral influence for both the static and traveling wave cases. The static case exhibits more intense turbulent spectral energy across a wide range of frequencies and wavenumbers, whereas the traveling wave case exhibits increased spectral energy localized about the actuation point itself. The fact that the static perturbation manifests a similar spatio-temporal spectral signature to the traveling wave perturbation is not entirely surprising, as the static waviness autonomously generates the equivalent of a traveling perturbation by shedding structures directly into the mean flow, to be advected downstream and reinforced by subsequent wavy elements.

Some caution should be exercised with these spectral comparisons across different flow scenarios due to the choice to align the cases in the velocity domain (matching local mean velocities) and not in the spatial domain (matching wall-normal locations). The implications of this choice require further investigation. Moreover, in both perturbed cases, the perturbation was not able to interact with a substantial amount of natural large-scales, due to the relatively low Reynolds number measured in these initial tests. Therefore, the precise nature of the phase-speed dependence of the large-scale interactions remains to be explored more fully. The key observation at low Reynolds number is how static waviness greatly exaggerates the effect of a traveling perturbation through the natural advection of the flow.

ACKNOWLEDGMENTS

The authors gratefully acknowledge the support of the US-Israel Binational Science Foundation grant 2022002. We also thank Eyal Barnea, Tal Tabachnick, Gal Porat, and our lab engineer, David Peles, for their tireless work designing and assembling the morphing surface.

REFERENCES

Akbarzadeh, A M & Borazjani, I 2020 Controlling Flow Separation on a Thick Airfoil Using Backward Traveling Waves. *AIAA Journal* **58** (9).

Alfredsson, P. H., Örlü, R., Kurian, T., Fransson, J. H. M., Segalini, A., Rüedi, J.-D. & Talamelli, A. 2009 The diagnostic plot - a new way to appraise turbulent boundary-layer data. In *Advances in Turbulence XII* (ed. B. Eckhardt), pp. 609–612.

Belcher, S. E. & Hunt, J. C. R. 1998 Turbulent flow over hills and waves. *Annu. Rev. Fluid Mechanics* **30** (November), 507–538.

Chavarin, A. & Luhar, M. 2020 Resolvent analysis for turbulent channel flow with riblets. *AIAA Journal* **58** (2), 589–599.

Cui, G. & Jacobi, I. 2023 Prediction of the phase difference between large-scale velocity and Reynolds stress fluctuations in wall turbulence. *Journal of Fluid Mechanics* **969**, 1–34.

Cui, G. & Jacobi, I. 2025 Interpretation of the amplitude modulation coefficient and a new transport-based coefficient. *J. Fluid Mechanics* **1002**, A35.

De Angelis, V, Lombardi, P & Banerjee, S 1997 Direct numerical simulation of turbulent flow over a wavy wall. *Physics of Fluids* **9** (8), 2429–2442.

Gatti, D., Quadrio, M., Chiarini, A., Gattere, F. & Pirozzoli, S. 2025 Turbulent skin-friction drag reduction via spanwise forcing at high Reynolds number. *Journal of Fluid Mechanics* **1016**, A58.

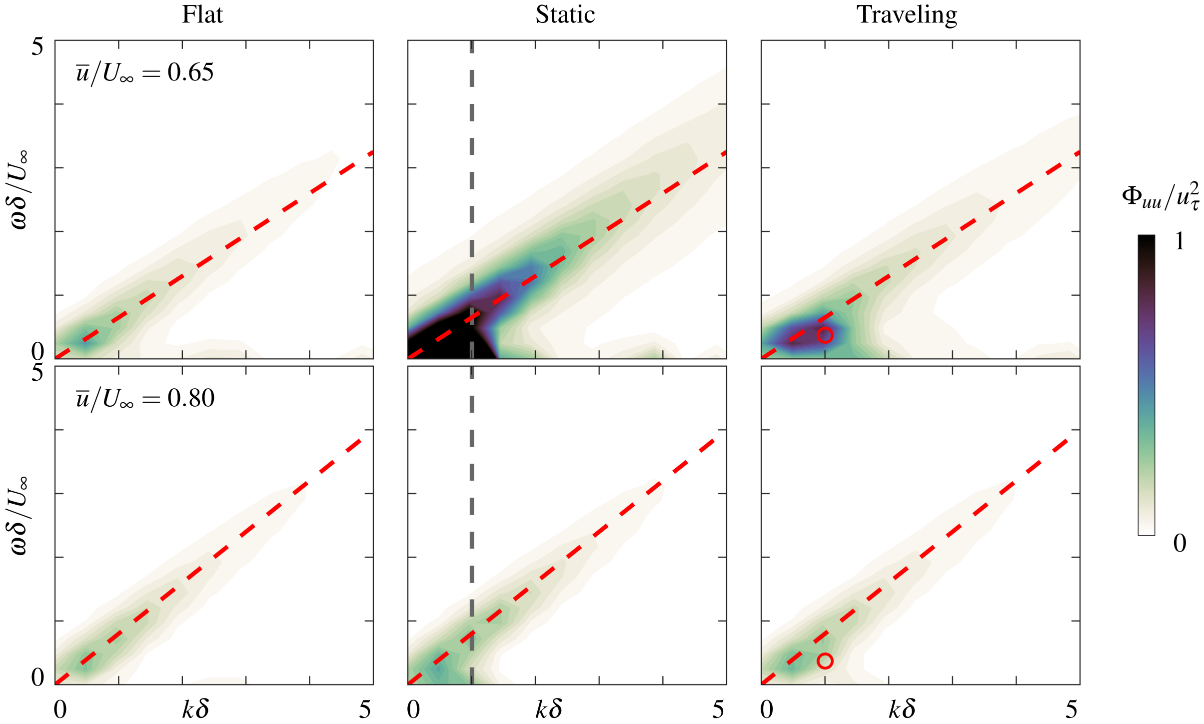

Figure 6. Space-time spectra, $\Phi_{uu}(k,\omega)$, for the three flow scenarios (columns) at different wall-normal positions where the local mean velocity was equal (rows). The wall-normal positions for $\overline{u}/U_\infty = 0.65$ were $y/\delta = (0.076, 0.149, 0.090)$ for the flat, static, and traveling cases, respectively. For $\overline{u}/U_\infty = 0.80$ they were $y/\delta = (0.304, 0.446, 0.372)$. The spectral densities are normalized by u_τ obtained for the flat wall case. The local mean velocity is marked by the red dashed line, the traveling wave actuation by the red circle, and the static wave by the black dashed line.

Jiménez, J. 2004 Turbulent flows over rough walls. *Annu. Rev. Fluid Mech.* **36**, 173–196.

Kruse, N., Günther, A. & von Rohr, P. R. 2003 Dynamics of large-scale structures in turbulent flow over a wavy wall. *J. Fluid Mechanics* **485**, 87–96.

Lee, J., Singh, A. & Guala, M. 2022 Reconstructing Sediment Transport by Migrating Bedforms in the Physical and Spectral Domains. *Water Resources Research* **58** (7).

Luhar, M., Sharma, A. S. & McKeon, B.J. 2015 A framework for studying the effect of compliant surfaces on wall turbulence. *Journal of Fluid Mechanics* **768**, 415–441.

Marusic, I., Chandran, D., Rouhi, A., Fu, M. K., Wine, D., Holloway, B., Chung, D. & Smits, A. J. 2021 An energy-efficient pathway to turbulent drag reduction. *Nature Communications* **12**, 5805.

Mathis, R., Hutchins, N. & Marusic, I. 2009 Large-scale amplitude modulation of the small-scale structures in turbulent boundary layers. *Journal of Fluid Mechanics* **628**, 311–337.

Mathis, R., Hutchins, N. & Marusic, I. 2011 A predictive inner–outer model for streamwise turbulence statistics in wall-bounded flows. *J. Fluid Mechanics* **681**, 537–566.

Nabae, Y., Kawai, K. & Fukagata, K. 2020 Prediction of drag reduction effect by streamwise traveling wave-like wall deformation in turbulent channel flow at practically high Reynolds numbers. *International J. Heat and Fluid Flow* **82** (January), 108550.

Reynolds, W. C. & Hussain, A. K. M. F. 1972 The mechanics of an organized wave in turbulent shear flow. part 3. theoretical models and comparisons with experiments. *J. Fluid Mechanics* **54** (2), 263–288.